MATERIALS ENGINEERING

Oil droplet self-transportation on oleophobic surfaces

2016 © The Authors, some rights reserved; exclusive licensee American Association for the Advancement of Science. Distributed under a Creative Commons Attribution NonCommercial License 4.0 (CC BY-NC).
10.1126/sciadv.1600148

Juan Li,[1] Qi Hang Qin,[2] Ali Shah,[3] Robin H. A. Ras,[2] Xuelin Tian,[2]* Ville Jokinen[1]*

Directional liquid transportation is important for a variety of biological processes and technical applications. Although surface engineering through asymmetric chemical modification or geometrical patterning facilitates effective liquid manipulation and enables water droplet self-transportation on synthetic surfaces, self-transportation of oil droplets poses a major challenge because of their low surface tension. We report oil droplet self-transportation on oleophobic surfaces that are microtextured with radial arrays of undercut stripes. More significantly, we observe three modes of oil motion on various sample surfaces, namely, inward transportation, pinned, and outward spreading, which can be switched by the structure parameters, including stripe intersection angle and width. Accompanying theoretical modeling provides an in-depth mechanistic understanding of the structure–droplet motion relationship. Finally, we reveal how to optimize the texture parameters to maximize oil droplet self-transportation capability and demonstrate spontaneous droplet movement for liquids down to a surface tension of 22.4 mN/m. The surfaces presented here open up new avenues for power-free liquid transportation and oil contamination self-removal applications in various analytical and fluidic devices.

INTRODUCTION

Many natural surfaces have directional liquid wetting and transportation properties, which allow cactuses (*1*) and spider silk (*2*) to collect fresh water from fog, and birds to shed water droplets off their feathers (*3*). On artificial surfaces, dynamic manipulation of droplets in a directional manner enables intelligent fluidic devices that hold diverse applications, including heat management (*4*), ink-jet printing (*5*), fluid diode (*6*, *7*), water harvesting (*8*, *9*), emulsion separation (*10*), and microanalysis (*11*–*13*). Asymmetric chemical modification (*4*, *14*–*16*) and geometrical patterning (*17*–*19*) are two general strategies for anisotropic liquid manipulation and even enable self-transportation of water droplets, which is highly useful for exploiting power-free fluidic devices that can operate in the absence of external energy input. Although significant advancements have been achieved for water droplet self-transportation (*14*–*19*), self-transportation of oils and other liquids with lower surface tensions remains a major challenge. Chemically patterned surfaces formed through the reactive formation of a molecular gradient usually show very limited contact angle difference at the front and back edges of oil droplets because of their much lower surface tension compared to water, resulting in insufficient driving force to overcome the hysteresis effect. On the other hand, oils usually tend to impregnate the texture on surfaces patterned with a geometrical gradient, making self-transportation infeasible. Lorenceau and Quéré (*20*) reported self-movement of oil droplets impaled on conical copper wires. However, because the copper wires were oleophilic, the droplet was in fact moving on an oil film, which means continuous loss of liquid during transport. Although Sumino and co-workers (*21*) demonstrated oil droplet self-running on a surface, the whole process involved continuous desorption and re-adsorption of surfactants and contamination of the oil droplet itself. Moreover, this droplet self-running occurred in the submerged oil-water system, which limits its applicability. Here, we report the self-transportation of oil droplets in ambient air on highly oleophobic, microtextured surfaces. In addition, we identify three distinct modes of droplet motion on the fabricated surfaces and explain through modeling the underlying mechanism. We further reveal how to optimize oil self-transportation capability through tuning the texture parameters.

RESULTS

Our surfaces have two essential structural features: radial arrays of microstripes and undercut profiles of each individual stripe (Fig. 1). The undercut structure plays a key role in supporting a low surface energy liquid such as oil and preventing it from wetting the texture (*22*, *23*). When an oil droplet is deposited on such surfaces, the solid-liquid-air contact line moves downward along the thin sidewall and stops at the lower edge of the undercut part (Fig. 1C) from where it provides an upward suspension force. Unlike microstripes with vertical walls, which can only support liquid with intrinsic contact angles θ_0 above 90°—this causes oil droplet transportation failure because no existing surfaces allow $\theta_0 > 90°$ with common oils (*22*, *24*, *25*)—the undercut structure in principle could provide a suspension force for any liquid with nonzero θ_0. Because the suspension force is quantified to be $\gamma l \sin\theta_0$ (γ is the liquid surface tension and l is the solid-liquid-air contact line length), we further coated the textured surfaces with fluoropolymer to increase θ_0 and maximize the suspension force to oil droplets. The undercut structure, together with fluoropolymer coating, can thus help achieve a robust Cassie-Baxter wetting mode (*26*) for oil droplets on the textured surface, enabling an air cushion in between to prevent oil from entering the texture. On the other hand, the radially arrayed geometry of microstripes creates a continuously decreasing air-liquid contact fraction (f_2) toward the center of the pattern for a Cassie-Baxter droplet (Fig. 1B), which, consequently, induces a continuous inward wettability gradient to drive droplet self-transportation because the apparent Cassie-Baxter contact angle increases with the air-liquid fraction (*19*, *26*). Moreover, unlike a discrete post or stripe

[1]Department of Materials Science and Engineering, Aalto University School of Chemical Technology, Tietotie 3, 02150 Espoo, Finland. [2]Department of Applied Physics, Aalto University School of Science, Puumiehenkuja 2, 02150 Espoo, Finland. [3]Department of Micro- and Nanosciences, Aalto University School of Electrical Engineering, Tietotie 3, 02150 Espoo, Finland.
*Corresponding author. Email: xuelin.tian@aalto.fi (X.T.); ville.p.jokinen@aalto.fi (V.J.)

Downloaded from http://advances.sciencemag.org/ on November 16, 2018

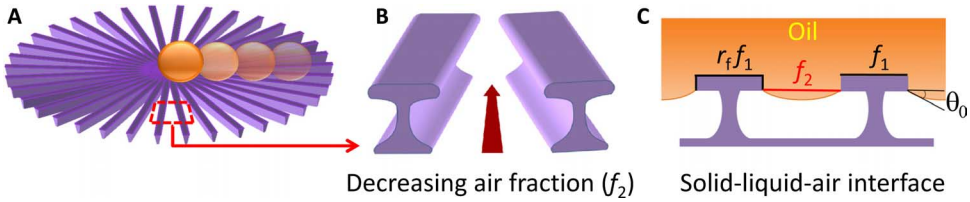

Fig. 1. Pattern design. (**A**) Schematic of the radially arrayed undercut microstripes for oil droplet self-transportation. (**B**) Radially continuously decreasing air-liquid contact fraction (f_2) creates an inward surface energy gradient. (**C**) Undercut structure with fluoropolymer coating maximizes upward suspension force for oil droplets, preventing penetration of oil into the texture.

design (*17*, *18*), our radial pattern allows continuous solid-liquid-air contact lines for inward droplet transportation, thus minimizing the hysteresis effect, which is the major obstacle for droplet motion. Therefore, oil droplets placed on the surface can move directionally toward the center of the pattern.

According to the above design requirements, we systematically prepared a series of surfaces composed of radially arrayed undercut microstripes (see Materials and Methods and fig. S1 for fabrication details). As shown in Fig. 2A, 12 samples with a stripe width D ranging from 7 to 17 μm, intersection angles Φ from 0.3125° to 5°, an undercut thickness h of ~0.5 μm, and a pattern radius of 4 mm are fabricated (see table S1 for detailed geometrical parameters). These samples are denoted as A1 to A5, B1 to B4, and C1 to C3, depending on the texture parameters D and Φ. Figure 2 (B to E) shows the structural details of pattern A4. The radial array of microstripes and the undercut cross-sectional profile of an individual stripe can be clearly observed. The thin undercut thickness minimizes the liquid-solid contact on the undercut sidewalls, which can improve the oleophobicity of the samples and reduce hysteresis resistance against droplet motion. The top surface and the thin undercut sidewalls have similar surface morphology, which exhibit nanoscale roughness due to TiO_2 coating (fig. S2) but have a flat appearance at the microscale, whereas the trough between two neighboring stripes exhibits highly rough topography.

Oil droplet transportation behaviors were evaluated by using hexadecane droplets (surface tension γ ~27.5 mN/m) as the model liquid, which were released onto the patterns 2.6 mm away from the center. Significantly, we observed three distinct modes of oil droplet motion on the prepared surfaces, and the results are summarized in different regimes in Fig. 3A. Typical time-lapse images of the three types of droplet behaviors are shown in Fig. 3B and movie S1. In the green regime of Fig. 3 (samples A4, A5, B3, B4, and C3), the oil droplet can move spontaneously from the outer area to the center (see A4 in Fig. 3B). No residual liquid film visible to the naked eye was left behind the droplet because of the Cassie-Baxter oleophobic state of the surfaces, although a thorough examination using a high-magnification optical microscope showed that a small amount of residual liquid remained nearby the pattern center (see fig. S3 and associated discussion), similar to what was observed on superomniphobic surfaces after droplet sliding or evaporation (*27*). Note that the oil droplet self-transportation demonstrated here is different from a previous report of oil transportation on azobenzene surfaces (*28*), which required light stimulation to drive liquid motion, whereas our surfaces enable spontaneous droplet motion without external energy input. The energy of the droplet motion comes from the excess free energy of adhesion released during its motion on the patterned surfaces caused by the gradient oil-air contact faction. The prepared surfaces have a long shelf life due to good chemical stability of the fluoropolymer coating, and we were able to use them for oil self-transport even after 10 months of storage under ambient conditions with no loss of performance.

In the blue regime of Fig. 3 (A3, B2, and C2), when the oil droplet is just touching the surface, it adopts a slightly asymmetric drop profile because of the inward wettability gradient. After the droplet is completely released, the relaxation of the droplet produces a slight inward displacement, but it immediately becomes pinned on the surface (see B2 in Fig. 3B). In the red regime of Fig. 3 (samples A1, A2, B1, and C1), an oil droplet readily spreads on the surface, and notably, the spreading direction is toward outside rather than inside (see A1 in Fig. 3B), indicating a motion mode in interesting contrast to that in the green regime.

DISCUSSION

To understand the above oil droplet motion behaviors, we calculated the contact angle θ of oil on the patterned surfaces according to the Cassie-Baxter model (*26*, *29*)

$$\cos\theta = r_f f_1 \cos\theta_0 - f_2 = r_f f_1 \cos\theta_0 - (1 - f_1) \quad (1)$$

where f_1 is the area fraction of the projected solid-liquid interface, r_f is the effective roughness of the wetted solid-liquid interface area (that is, the ratio of wetted area and its projection area), and θ_0 is the contact angle on a planar surface with identical surface chemistry to the structured surface. In our experiments, the oil contact angle on a flat surface with a TiO_2 layer and a fluoropolymer coating is 55° (fig. S2). Because θ_0 is less than 90°, the solid-oil-air contact line stops at the lower edge of the sidewall (Fig. 1C). In such a configuration, f_1 is R/L, and $r_f f_1$ is calculated to be $R/L + 2h/\Phi L$. The apparent contact angle θ is thus determined: $\cos\theta = (R/L + 2h/\Phi L)\cos\theta_0 - (1 - R/L)$, where $R \leq L \leq 4$ mm. Because $R = D/\Phi$, we can get

$$\theta = \begin{cases} \arccos\left[\left(\frac{D}{\Phi L} + \frac{2h}{\Phi L}\right)\cos\theta_0 - \left(1 - \frac{D}{\Phi L}\right)\right] & (D/\Phi \leq L \leq 4\text{mm}) \\ \theta_0 & (0 \leq L \leq D/\Phi) \end{cases} \quad (2)$$

Function curves showing the relationship between θ and L are plotted in Fig. 4A, which can be classified into three groups (indicated by different colors), corresponding to three types of droplet behaviors. The surfaces in the green group (A4, A5, B3, B4, and C5) show relatively lower contact angles than the other two groups of samples, and more importantly,

Downloaded from http://advances.sciencemag.org/ on November 16, 2018

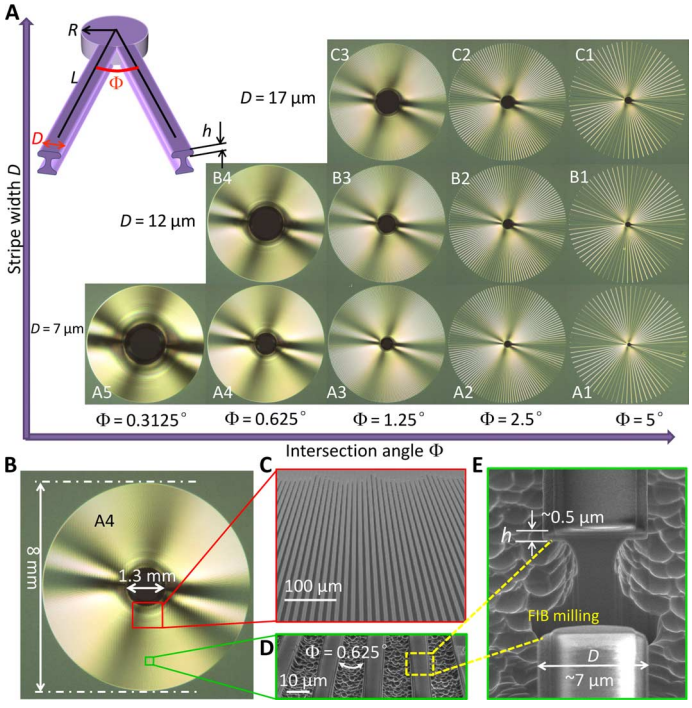

Fig. 2. The fabricated patterns composed of radially arrayed undercut microstripes. (**A**) Photographs of 12 samples with systematically varied parameters. Inset: Schematic illustration of the two neighboring stripes with the undercut structure. *D* is the stripe width, Φ is the intersection angle between two neighboring stripes, *R* is the radius of the central circle formed by intersection of the stripes, *h* is the undercut thickness, and *L* is the distance to the center. (**B** to **E**) Structure details of a typical A4 sample. (C) Scanning electron microscope (SEM) image near the center shows radially arrayed microstripes. (D) Magnified image of the radial stripes far from the center. (E) Cross-sectional view of an individual stripe reveals the undercut profile. The stripe was locally removed by focused ion beam (FIB) milling to expose the cross-sectional morphology.

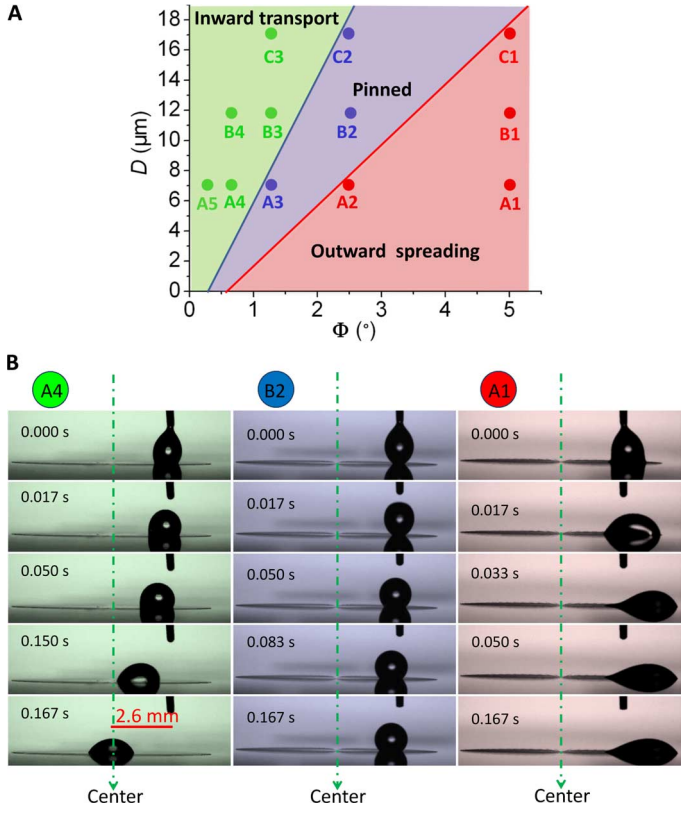

Fig. 3. Three modes of oil droplet motion on different patterns. (**A**) Regime diagram showing three types of oil droplet behaviors depending on pattern parameters. In the green regime, oil droplets move spontaneously toward the center. In the blue regime, oil droplets remain pinned after being released. In the red regime, oil droplets exhibit outward spreading. The test liquid is hexadecane and the droplet volume is fixed at 1 μl. (**B**) Time-lapse images illustrating the three modes of oil droplet motion.

these surfaces have steeper wettability gradients than the other two groups at the outer area of the patterns (2 mm < *L* < 4 mm). On the basis of an interfacial free energy argument, the driving force for droplet motion on gradient surfaces scales as $F_d = -\pi r^2 \gamma d(\cos\theta)/dL$, where *r* is the base radius of the droplet (*30*). Thus, $-d(\cos\theta)/dL$ can be used as a characteristic parameter to evaluate the driving force of different surfaces. On the patterned area, we can get

$$-\frac{d(\cos\theta)}{dL} = \frac{D(1+\cos\theta_0)+2h\cos\theta_0}{L^2\Phi} \quad (3)$$

The $-d(\cos\theta)/dL$ versus *L* curves of different patterns are plotted in Fig. 4B. The green group of samples exhibits the largest $-d(\cos\theta)/dL$, which thus provides sufficient driving force to overcome the hysteresis effect. This explains why only the green group can initiate the inward self-motion of oil droplets. Moreover, the relatively small contact angles on the green group of samples give a larger base radius *r* for droplets, which also benefits droplet motion because the driving force $F_d \propto r^2$, whereas the hysteresis force $F_h \propto r$ (*31*). It is worth mentioning that the liquid transport is limited to the radial length of the stripes, and meanwhile, the stripes cannot be too long such that the droplet size is well above the maximum separation between two neighboring stripes. For the blue group of samples in Fig. 4, the less steep wettability gradient is insufficient to drive the motion of oil droplets, which thus remain pinned on the surfaces.

For the red group of samples in Fig. 4 (A1, A2, B1, and C1), the upward suspension force provided by the undercut structure turns out to be insufficient for creating a robust solid-air composite interface to support oil droplets, and consequently, the oil droplets readily undergo a transition to the Wenzel state (*32*); that is, the liquid penetrates the texture. The breakthrough pressure P_c for oil to penetrate the texture can be quantified as

$$P_c = \frac{2\gamma\sin\theta_0}{L\Phi - D} \quad (4)$$

Tuteja *et al.* proposed that $P_{ref} = 2\gamma/l_{cap}$ can be used to estimate the minimum pressure of a droplet exerted on a highly hydrophobic/oleophobic surface, where $l_{cap} = \sqrt{\gamma/\rho g}$ is the capillary length of the liquid (~1.9 mm for hexadecane) (*22*, *33*). Hence, we can use P_c/P_{ref} as a dimensionless parameter to evaluate the robustness of different patterns to support

Downloaded from http://advances.sciencemag.org/ on November 16, 2018

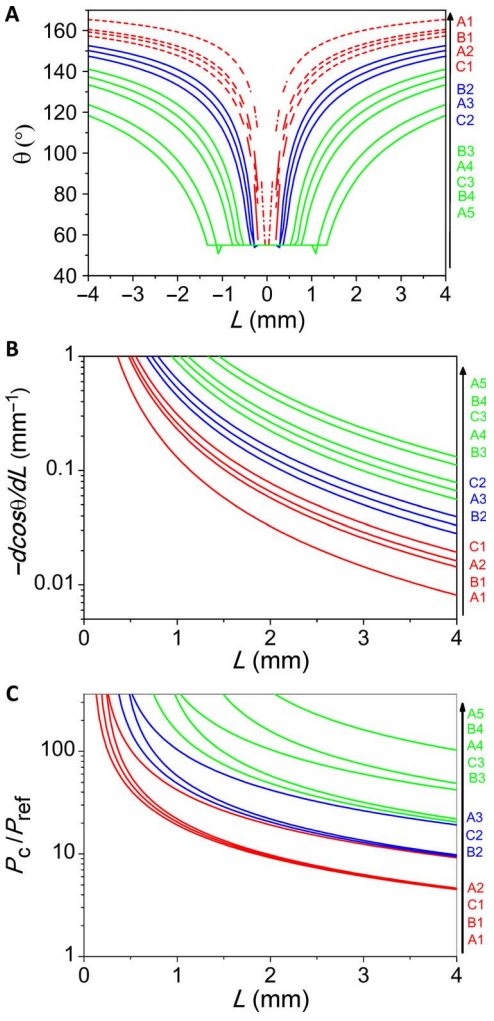

Fig. 4. Mechanistic understanding. (**A** to **C**) Calculated oil contact angle θ (A), wettability gradient $-d(\cos\theta)/dL$ (B), and breakthrough pressure P_c/P_{ref} (C) curves as functions of L on the 12 patterned surfaces. Different curve colors correspond to the three modes of droplet motion. The red curves in (A) are shown in dashed lines because oil droplets tend to collapse into the Wenzel state in this regime.

Cassie state oil droplets. The red group of samples is located at the bottom right regime of Fig. 3A, that is, the area with the largest Φ and smallest D values, which thus give much smaller P_c/P_{ref} values compared to the other two groups (Fig. 4C). For example, at the outmost location (L = 4 mm), A1 only gives a P_c/P_{ref} of around 4.6, whereas A5 has a P_c/P_{ref} of as high as 105. This explains why oil droplets collapse easily into the Wenzel state on the red group of samples. Moreover, when an oil droplet collapses, its outer side collapses more easily than the inner side because the outer side contacts microstripes with a larger interspace, which means less P_c to prevent collapse occurrence (fig. S4). Therefore, the collapse initiates from the outer side, and such asymmetric collapse results in the outward spreading of oil droplets.

Finally, we discuss the parameter requirements for optimizing the oil droplet self-transportation ability of the patterns. The key is to maximize the driving force F_d and the breakthrough pressure P_c to avoid droplet pinning or collapse events. From Eq. 3, we obtain $F_d \propto f(D, \Phi) = [D(1 + \cos\theta_0) + 2h\cos\theta_0]/\Phi$. As $f(D, \Phi)$ decreases with Φ and increases with D (fig. S5), F_d can thus be optimized by reducing Φ and increasing D. From Eq. 4, it is clear that P_c also decreases with Φ and increases with D. Therefore, we can conclude that the pattern design can be optimized by simultaneously minimizing Φ and maximizing D. This also explains why the green regime in Fig. 3A is located at the top left corner where both Φ and D are optimized so that oil droplets can readily move inward, whereas the red regime is at the bottom right corner where the lowest P_c is obtained and droplets tend to collapse into the Wenzel state, and the blue regime is located in between where droplets do not move or collapse. In practical fabrication, Φ is restricted by the machining precision of the microfabrication/nanofabrication technique and cannot be infinitely reduced, and D cannot exceed the product of pattern radius and Φ.

On the basis of the theoretical consideration presented above, samples A4, A5, B3, B4, and C3 (marked green in Figs. 3 and 4) were identified as the most promising. Every sample in this group was able to sustain the Cassie state of droplets of various surface tensions down to a surface tension of 27 mN/m and spontaneously move them along the radial gradient. This capability is demonstrated in fig. S6 and movie S2 for sample B3, which had the lowest driving force (Fig. 4B) and the lowest breakthrough pressure (Fig. 4C) of the samples in the green group. On the other hand, sample A5, which has the highest driving force and breakthrough pressure, can drive an even broader range of liquids. Even an ethanol droplet (99.5%, γ ~22.4 mN/m) can move spontaneously on such a pattern (fig. S7 and movie S3). We also investigated the effect of pattern parameters and liquid type on droplet speed. For different patterns in the green group, the transport speed of a 3-μl hexadecane droplet changes from 2.98 to 2.40 cm/s (see table S2), which is caused by their difference in wettability gradient (Fig. 4B). In contrast, the effect of liquid type is less pronounced, and the speed shows a slight increase with decreased liquid surface tension, attributed to the increased droplet contact radius (see table S3).

CONCLUSION

We have demonstrated directional self-transportation of oil droplets on oleophobic surfaces composed of radially arrayed undercut stripes. Moreover, three modes of droplet motion are observed and the underlying mechanism is explained. The oil droplet self-transportation capability of the surfaces can be optimized by reducing the stripe intersection angles or by increasing the stripe width. The radially arrayed undercut microstripe patterns allow alignment of oil droplets to a central point. This property could be used for power-free and self-aligned liquid transportation for various analytical devices because many chemical and biological samples have surface tensions much lower than that of pure water. Alternatively, it could be used to eliminate oil or ink accumulation and contamination in fluid devices by transporting stray droplets away from peripheral areas, for example, as an anti-clogging solution for ink-jet printheads.

MATERIALS AND METHODS

Surface fabrication

The fabrication process of the surfaces is shown in fig. S1. First, a 1-μm-thick SiO_2 layer was deposited on a silicon wafer (525-μm-thick p-type

Downloaded from http://advances.sciencemag.org/ on November 16, 2018

⟨1 0 0⟩) by plasma-enhanced chemical vapor deposition (PECVD). The SiO_2 layer was patterned by photolithography and reactive ion etching (RIE). After photoresist removal, anisotropic etching (4 min) and isotropic etching (6 min) of silicon were carried out via cryogenic deep reactive ion etching [inductively coupled plasma (ICP)–RIE]. It should be noted that around 500 nm of SiO_2 was etched during the whole ICP-RIE process. Next, atomic layer deposition was used to deposit a 50-nm-thick TiO_2 film. Finally, an 80-nm-thick fluoropolymer layer was coated in CHF_3 plasma by PECVD.

Structure characterization

FIB milling and cross-sectional SEM investigation were performed in an SEM/FIB dual-beam microscope [Helios NanoLab 600; the equipment combines an SEM and an FIB (Ga^+) microscope]. Other SEM images were taken by a Supra 40 field emission SEM (Zeiss).

Contact angle and droplet motion investigations

Contact angles and oil droplet motion were investigated using an Attension Theta goniometer (Biolin Scientific) equipped with a camera. To dispense droplets, a 30-gauge flat-tipped needle coated with fluoropolymer was used to facilitate the deposition of oil droplets. The motion of droplets on the surfaces was recorded with the built-in camera at a rate of 60 frames per second.

Sample cleaning in case of oil contamination

Oil contamination on top of the stripes does not prevent oil droplet self-transportation. However, in case oil contamination enters the grooves, the sample needs to be cleaned before self-transportation. The surface can be cleaned by first washing it with common organic solvents (for example, ethanol, isopropanol, or acetone) and then vacuum-drying it at 120°C for 12 hours.

SUPPLEMENTARY MATERIALS

Supplementary material for this article is available at http://advances.sciencemag.org/cgi/content/full/2/6/e1600148/DC1

fig. S1. Fabrication process flow for the radial undercut patterns with TiO_2 and polymer coatings.
fig. S2. SEM images and contact angles of TiO_2 and fluoropolymer-coated surfaces and merely fluoropolymer-coated surfaces.
fig. S3. Optical images of residual liquid on sample B3 after droplet transport.
fig. S4. The outward spreading of an oil droplet of 1 μl on the A1 pattern.
fig. S5. The effect of D and Φ on the driving force for droplet motion.
fig. S6. Self-transportation of water-ethanol mixture droplets of different compositions on sample B3.
fig. S7. Self-transportation of an ethanol droplet on sample A5.
table S1. Geometrical parameters of different patterns and their contact angles, wettability gradients, and breakthrough pressure equations.
table S2. Effect of pattern parameters on droplet speed.
table S3. Effect of liquid type on droplet speed.
movie S1. Demonstration of three modes of oil droplet motion on various sample surfaces.
movie S2. Self-transportation of ethanol-water mixture droplets with different compositions on sample B3.
movie S3. Self-transportation of an ethanol droplet on sample A5.

REFERENCES AND NOTES

1. J. Ju, H. Bai, Y. Zheng, T. Zhao, R. Fang, L. Jiang, A multi-structural and multi-functional integrated fog collection system in cactus. *Nat. Commun.* **3**, 1247 (2012).
2. Y. Zheng, H. Bai, Z. Huang, X. Tian, F.-Q. Nie, Y. Zhao, J. Zhai, L. Jiang, Directional water collection on wetted spider silk. *Nature* **463**, 640–643 (2010).
3. R. J. Kennedy, Directional water-shedding properties of feathers. *Nature* **227**, 736–737 (1970).
4. S. Daniel, M. K. Chaudhury, J. C. Chen, Fast drop movements resulting from the phase change on a gradient surface. *Science* **291**, 633–636 (2001).
5. O. Bliznyuk, J. R. T. Seddon, V. Veligura, E. S. Kooij, H. J. W. Zandvliet, B. Poelsema, Directional liquid spreading over chemically defined radial wettability gradients. *ACS Appl. Mater. Interfaces* **4**, 4141–4148 (2012).
6. X. Tian, H. Jin, J. Sainio, R. H. A. Ras, O. Ikkala, Droplet and fluid gating by biomimetic janus membranes. *Adv. Funct. Mater.* **24**, 6023–6028 (2014).
7. A. Groisman, S. R. Quake, A microfluidic rectifier: Anisotropic flow resistance at low Reynolds numbers. *Phys. Rev. Lett.* **92**, 094501 (2004).
8. E. Kang, G. S. Jeong, Y. Y. Choi, K. H. Lee, A. Khademhosseini, S.-H. Lee, Digitally tunable physicochemical coding of material composition and topography in continuous microfibres. *Nat. Mater.* **10**, 877–883 (2011).
9. X. Tian, Y. Chen, Y. Zheng, H. Bai, L. Jiang, Controlling water capture of bioinspired fibers with hump structures. *Adv. Mater.* **23**, 5486–5491 (2011).
10. K. Li, J. Ju, Z. Xue, J. Ma, L. Feng, S. Gao, L. Jiang, Structured cone arrays for continuous and effective collection of micron-sized oil droplets from water. *Nat. Commun.* **4**, 2276 (2013).
11. K.-H. Chu, R. Xiao, E. N. Wang, Uni-directional liquid spreading on asymmetric nanostructured surfaces. *Nat. Mater.* **9**, 413–417 (2010).
12. V. Jokinen, M. Leinikka, S. Franssila, Microstructured surfaces for directional wetting. *Adv. Mater.* **21**, 4835–4838 (2009).
13. N. A. Malvadkar, M. J. Hancock, K. Sekeroglu, W. J. Dressick, M. C. Demirel, An engineered anisotropic nanofilm with unidirectional wetting properties. *Nat. Mater.* **9**, 1023–1028 (2010).
14. M. K. Chaudhury, G. M. Whitesides, How to make water run uphill. *Science* **256**, 1539–1541 (1992).
15. D. Hong, W. K. Cho, B. Kong, I. S. Choi, Water-collecting capability of radial-wettability gradient surfaces generated by controlled surface reactions. *Langmuir* **26**, 15080–15083 (2010).
16. H. S. Khoo, F.-G. Tseng, Spontaneous high-speed transport of subnanoliter water droplet on gradient nanotextured surfaces. *Appl. Phys. Lett.* **95**, 063108 (2009).
17. J.-T. Yang, Z.-H. Yang, C.-Y. Chen, D.-J. Yao, Conversion of surface energy and manipulation of a single droplet across micropatterned surfaces. *Langmuir* **24**, 9889–9897 (2008).
18. H. K. Bardaweel, K. Zamuruyev, J.-P. Delplanque, C. E. Davis, Retraction: Wettability-gradient-driven micropump for transporting discrete liquid drops. *J. Micromech. Microeng.* **23**, 035036 (2013).
19. J. Li, X. Tian, A. P. Perros, S. Franssila, V. Jokinen, Self-propelling and positioning of droplets using continuous topography gradient surface. *Adv. Mater. Interfaces* **1**, 1400001 (2014).
20. É. Lorenceau, D. Quéré, Drops on a conical wire. *J. Fluid Mech.* **510**, 29–45 (2004).
21. Y. Sumino, N. Magome, T. Hamada, K. Yoshikawa, Self-running droplet: Emergence of regular motion from nonequilibrium noise. *Phys. Rev. Lett.* **94**, 068301 (2005).
22. A. Tuteja, W. Choi, M. Ma, J. M. Mabry, S. A. Mazzella, G. C. Rutledge, G. H. McKinley, R. E. Cohen, Designing superoleophobic surfaces. *Science* **318**, 1618–1622 (2007).
23. V. Liimatainen, V. Sariola, Q. Zhou, Controlling liquid spreading using microfabricated undercut edges. *Adv. Mater.* **25**, 2275–2278, 2274 (2013).
24. D. Quéré, Wetting and roughness. *Annu. Rev. Mater. Res.* **38**, 71–99 (2008).
25. T. L. Liu, C.-J. C. Kim, Turning a surface superrepellent even to completely wetting liquids. *Science* **346**, 1096–1100 (2014).
26. A. B. D. Cassie, S. Baxter, Wettability of porous surfaces. *Trans. Faraday Soc.* **40**, 546–551 (1944).
27. R. Dufour, P. Brunet, M. Harnois, R. Boukherroub, V. Thomy, V. Senez, Zipping effect on omniphobic surfaces for controlled deposition of minute amounts of fluid or colloids. *Small* **8**, 1229–1236 (2012).
28. K. Ichimura, S.-K. Oh, M. Nakagawa, Light-driven motion of liquids on a photoresponsive surface. *Science* **288**, 1624–1626 (2000).
29. A. Marmur, Wetting on hydrophobic rough surfaces: To be heterogeneous or not to be? *Langmuir* **19**, 8343–8348 (2003).
30. S. Daniel, S. Sircar, J. Gliem, M. K. Chaudhury, Ratcheting motion of liquid drops on gradient surfaces. *Langmuir* **20**, 4085–4092 (2004).
31. G. Macdougall, C. Ockrent, Surface energy relations in liquid/solid systems. I. The adhesion of liquids to solids and a new method of determining the surface tension of liquids. *Proc. R. Soc. London Ser. A* **180**, 151–173 (1942).
32. R. N. Wenzel, Resistance of solid surfaces to wetting by water. *Ind. Eng. Chem.* **28**, 988–994 (1936).
33. A. Tuteja, W. Choi, J. M. Mabry, G. H. McKinley, R. E. Cohen, Robust omniphobic surfaces. *Proc. Natl. Acad. Sci. U.S.A.* **105**, 18200–18205 (2008).

Acknowledgments: This work was performed at the Micronova Nanofabrication Centre of Aalto University. We thank A. Peltonen for his help in FIB milling and I. Díez for her help in optical microscopy investigation. **Funding:** This work was financially supported by the Academy of Finland through its Centres of Excellence Programme (2014–2019) and under project nos. 266820,

Downloaded from http://advances.sciencemag.org/ on November 16, 2018

263560, and 283210 and the Aalto University School of Chemical Technology (postdoctoral grant to J.L.). **Author contributions:** J.L., X.T., and V.J. designed the research; J.L., Q.H.Q., and A.S. conducted the experiments; J.L. and X.T. performed the theoretical calculations; and J.L., R.H.A.R., X.T., and V.J. wrote the paper. **Competing interests:** The authors declare that they have no competing interests. **Data and materials availability:** All data needed to evaluate the conclusions in the paper are present in the paper and/or the Supplementary Materials. Additional data related to this paper may be requested from the authors.

Submitted 26 January 2016
Accepted 26 May 2016
Published 17 June 2016
10.1126/sciadv.1600148

Citation: J. Li, Q. H. Qin, A. Shah, R. H. A. Ras, X. Tian, V. Jokinen, Oil droplet self-transportation on oleophobic surfaces. *Sci. Adv.* **2**, e1600148 (2016).

Downloaded from http://advances.sciencemag.org/ on November 16, 2018

Science Advances

Oil droplet self-transportation on oleophobic surfaces

Juan Li, Qi Hang Qin, Ali Shah, Robin H. A. Ras, Xuelin Tian and Ville Jokinen

Sci Adv **2** (6), e1600148.
DOI: 10.1126/sciadv.1600148

ARTICLE TOOLS http://advances.sciencemag.org/content/2/6/e1600148

SUPPLEMENTARY MATERIALS http://advances.sciencemag.org/content/suppl/2016/06/14/2.6.e1600148.DC1

REFERENCES This article cites 33 articles, 7 of which you can access for free
http://advances.sciencemag.org/content/2/6/e1600148#BIBL

PERMISSIONS http://www.sciencemag.org/help/reprints-and-permissions

Use of this article is subject to the Terms of Service

Science Advances (ISSN 2375-2548) is published by the American Association for the Advancement of Science, 1200 New York Avenue NW, Washington, DC 20005. 2017 © The Authors, some rights reserved; exclusive licensee American Association for the Advancement of Science. No claim to original U.S. Government Works. The title *Science Advances* is a registered trademark of AAAS.

Downloaded from http://advances.sciencemag.org/ on November 16, 2018